Chemical Science

Accepted Manuscript

This article can be cited before page numbers have been issued, to do this please use: M. Zhao, T. Li, C. Li, H. Huang, Y. Wang, L. Dong, X. Shi, Y. Wu, G. Hao and A. Lu, *Chem. Sci.*, 2025, DOI: 10.1039/D5SC04466A.

ROYAL SOCIETY OF CHEMISTRY

rsc.li/chemical-science

View Article Online
DOI: 10.1039/D5SC04466A

ARTICLE

Large-area, flexible, and conductive porous film of interlinked carbon nanospheres for UV light filter and resistive heater

Received 00th January 20xx,
Accepted 00th January 20xx

DOI: 10.1039/x0xx00000x

Meng-Qi Zhao[‡a], Tian-Yi Li[‡a], Chuan-Bin Li[‡a], Hui-Qun Huang[a], Yong-Sheng Wang[a], Ling-Yu Dong[a], Xiao-Dong Shi[a], Yu-Tai Wu[a], Guang-Ping Hao*[a], and An-Hui Lu*[a]

Abstract: Conductive and flexible thin film is promising for wearable electronic devices, and is challenging in fabrication due to its multiple requirements on structural and functional integration. Here, we present a chemical method for the preparation of large-area carbon film by *in situ* linking uniform carbon nanospheres that derived from stiff-shell polymeric crystals. The proof-of-concept interlinked carbon film features a dual-porous structure, consisting of the intrinsic micropores within the nodes of carbon spheres and the in-plane macropores within the interlinked carbon spheres patterned in mono-/few layer. The success in preparation of such interlinked carbon film relies on the unique combination of the liquid-solid configuration of polymeric stiff-shell and soft core, which induce a series of dynamic transformation from phase expansion, fusion, linking, and eventually form large-area interlinked porous carbon nanospheres patterned in one layer. Such thin carbon films can be transferred onto various rigid or flexible substrates, and perform well as light filter that can block > 90% UV light, as electrical-heating material that delivered a heating efficiency up to 45.8 °C/μm. This work provides a smart engineering platform and benefit the design of future electronic skin and intelligent wearable devices.

Introduction

Large-area, flexible, and conductive porous carbon films have attracted considerable research interest for optical and thermal management applications, driven by the ongoing trend toward miniaturization and integration in electronic devices.[1-5] As optical functional materials, monolayer nanocarbon material is one important option due to their lightweight and tunable microstructures.[6,7] However, conventional nanocarbon materials exhibit limited spectral tenability. For instance, high-quality single-layer graphene films show near-complete light transmission,[8] while other nanocarbons, e.g., carbon nanospheres, display the full-band absorption properties,[9] making the selective light-filtering highly difficult. For personal thermal management, it demands wearable Joule heaters, for which a thin conductive carbon film with high thermal conductivity is ideally required.[10,11] Integrating both functions in one film material is highly challenging, which calls for targeted structural design of naoncarbons at both the microscopical and macroscopical level.

From microscopic aspect, the surface/interface structures of nanocarbons would improve the selective light absorption or scattering.[12,13] In particular, surface structure with nano-patterns is one typical feature that could increase the accessible area, facilitate encoding surface properties,[14,15] thus tuning optical characteristics.[16-19] To date, various methods were explored to engineer fine surface structures in carbon spheres, which include emulsion polymerization,[20] surface coating,[21] and other post-modifications.[22] From macroscopic aspect of a monolayer nanocarbon assembly, it needs to connect all the individual nanocarbons into a complete film, which not only ensures the electron conductivity, but also preserves selective light transmission pathways. Although significant advances have been made in developing diverse nanocarbon materials,[23-29] few studies can fulfil both of the aforementioned requirements.

Herein, we developed a chemical mimicry approach to construct a stiff-shell, soft-core polymeric structure, which spontaneously evolves into interlinked porous carbon nanospheres patterned in large-area monolayer film. For the core material, thermotropic polymer such as liquid crystals were reasonably employed considering their soft crystalline feature,[30,31] which potentially reveal favorable melting properties and thus create interactions between particles upon heating. Meanwhile, the highly crosslinked and stiff polymers were proposed as shell material that can resist the complete meltdown during thermal treatment.[32] We showcased the fine control of the formation of the two components in spite of their fast and competitive reaction kinetics between nucleation and subsequent polymerization.[33,34] The devised large-area monolayer film composed of interlinked nanocarbon spheres with controllable surface structures are well beyond the conventional nanocarbon films with multifunctionality that can effectively filter > 90% UV light and enable thin and wearable Joule heating.

[a] State Key Laboratory of Fine Chemicals, Frontier Science Center for Smart Materials, Liaoning Key Laboratory for Catalytic Conversion of Carbon Resources, and School of Chemical Engineering. Dalian University of Technology. Dalian 116024, P. R. China. E-mail: guangpinghao@dlut.edu.cn (G.-P. H.), anhuilu@dlut.edu.cn (A.-H. L.)

‡ M.-Q. Z., T.-Y. L. and C.-B. L. contribute equally.

† Electronic supplementary information (ESI) available.

View Article Online
DOI: 10.1039/D5SC04465A

Results and Discussion

The synthesis of quasi-liquid polymeric crystals (LPCs) is based on the rapid formation of Schiff-based liquid crystals as initial seeds, surrounding which highly crosslinked polymer shells *in situ* grow (**Figure 1a, left**). The heterogeneous stiff-shell and soft-core structure forms in one-step in solution phase via cascading polymerization between Schiff-base seeds and benzoxazine monomers. First, the Schiff-base condensation between terephthalaldehyde (TPA) and *p*-phenylenediamine (*p*-PDA) initiates the rapid chain propagation and thus a fast nucleation at the early stage, owing to the highly reactive nucleophilic addition of aromatic amine to carbonyl group.[35] The π-π stacking and rigid C=N bonds ensures the ordered arrangement of molecular chains, endowing the core with soft polymeric structure.[36] Subsequently, the unoccupied -NH_2 in the outer layer of the Schiff-base core provides ample heterogeneous nucleation sites for Mannich reaction upon introducing *p*-hydroquinone (HQ). During subsequent aging, the networks in the outer layer further crosslink, ending with the formation of dense stiff shell. Upon heating, the highly uniform and monolayer LPCs sequentially expanded, fused, shrank, and transformed into interlinked nanocarbon monolayer film (denoting MLCF, **Figure 1a right**).

We also screened different kinds of amines and phenols for this synthesis (**Figure S1-S3**), which failed to form such uniform nanospheres. This indicates that the reaction at the para-position of TPA, *p*-PDA, and HQ is unique for the tri-component reactions and subsequent distribution of the soft and hard components. Notably, this self-assembly strategy exhibits exceptional substrate universality, which enables the formation of high-quality film over diverse substrates including silicon wafers, quartz glass, and flexible polyethylene terephthalate (PET) (**Figure 1b, Figure S4**). In addition, by controlling the thermal treatment conditions, nanocarbons in dispersed powder form can also be prepared, which denote DPC.

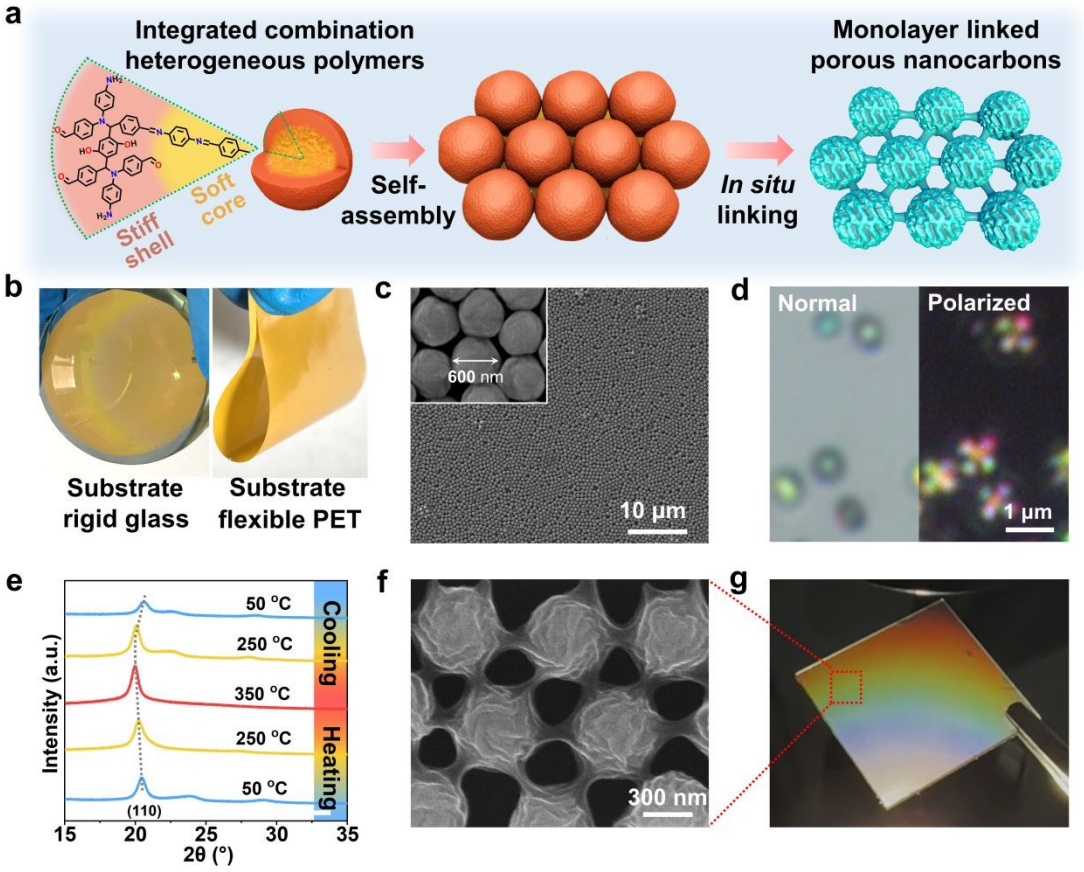

Figure 1 Illustration and morphological characterizations of LPCs and MLCF. (a) Schematic of the synthesis of LPCs and monolayer interlinked nanocarbon film. (b) Monolayer coating of the LPCs on substrates of glass and plastic of PET. (c) SEM image of the LPCs. Inset: high magnification image. (d) Optical microscopy images of LPCs with normal light and cross-polarized light. (e) *In situ* PXRD patterns during reversibly thermal treatment. (f) SEM image of the monolayer film of interlinked nanocarbon spheres. (g) Optical image of the monolayer film of interlinked nanocarbon spheres under light emitting diode. The SEM images in (c, f) and optical images in (d, g) were collected at room temperature.

The scanning electron microscopy (SEM) images confirm that the resultant LPCs are highly uniform spheres with size of ~600 nm in diameter (**Figure 1c**). The images of transmission electron microscopy (TEM) and scanning electron microscope-focused ion beam (SEM-FIB) reveal that the LPCs are solid structure (**Figure S5**). Notably, the LPCs are not standard spheroids, but rather deformable due to the quasi-liquid nature of the soft core. The crystalline feature of the LPCs was first evaluated by cross-polarized optical microscopy (**Figure 1d, Figure S6**). A dark cross (known as "Maltese cross") was observed on LPCs, which is typical feature of spherulites. Spherulites are spherical polymer crystals with radially aligned crystalline polymer lamellae.[37] This observation suggests that the soft-core of

View Article Online
DOI: 10.1039/D5SC04465A

LPCs is essentially the nano-sized Schiff-base sheets assembled in spherical configurations.

Powder X-ray diffraction (PXRD) studies were conducted to further identify the crystal structure of LPCs. *In situ* XRD patterns were collected in a temperature range from 50 °C to 350 °C, and then back to 50 °C (**Figure 1e**). The phase structures are consistent with the reported Schiff-base materials.[38] The relatively sharp diffraction peak at 2θ of 20.4° coincides with the (110) planes of Schiff-base crystals. When the temperature increases to 350 °C, LPCs still largely preserve its crystalline structure, while the (110) plane at 20.4° moves to lower angles, indicating the thermally induced cell expansion. The structure change is highly reversible in the tested temperature range. We did not observe visible morphological changes of LPCs after the temperature cycling, which confirmed their structural stability (**Figure S7**).

We then assembled the LPCs into monolayer film on silicon (Si) wafer (**Figure S8**). The thermal treatment of the LPCs patterned in monolayer manner at 800 °C led to the formation of the nanocarbon films. To our surprise, we observed two unique features of such nanocarbon films. One is its unique morphology with uniform surface folding with depth of 20~40 nm determined by atomic force microscopy (**Figure S9, Figure 1f**). This is distinct to common homogeneous polymer precursors, which resulted in smooth surface (**Figure S10**). Previous simulation and experimental results at macroscopic scale suggest that such gyrus-like nanofolds may arise from the joint effect of bending the hard shell and compressing the soft-core.[39-41] We speculate that the non-synchronous structure transformation for LPCs followed similar way due to the induced stress difference during heating. The structural evolution will be discussed in the next section of the formation mechanism. The other feature is that the nanocarbon spheres in monolayer are interlinked with each other (**Figure S11**). Each nanocarbon sphere functions as a node and connects with its neighboring by "nano-necks" (**Figure 1f**). The formation of the nano-necks is likely stemmed from the melting Schiff-base core, which seep through the softening shell during heating. In this way, the monolayer carbon nanospheres were interlinked, forming an entire and complete film (MLCF). We transferred the MLCF to the flexible and transparent subtract of polydimethylsiloxane (PDMS). The obtained PDMS supported MLCF is rather transparent. Moreover, the digital camera image shows that the film displays vivid grating colors under light (**Figure 1g**). This can be interpreted that the wavelengths of light are selectively propagated upon interaction with periodically arranged micron or submicron structures, which also indicates the uniform size of the nanocarbon nodes. Notably, the large area film exhibited electron conductive property (**Figure S12**), suggesting its structural integrity with the interlinked feature.

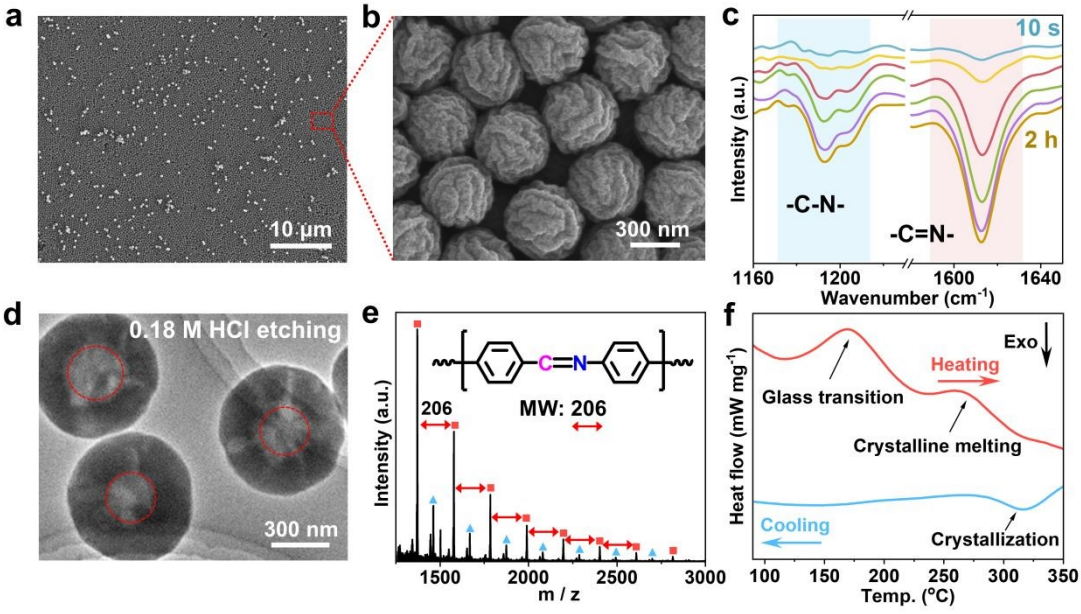

Figure 2 Chemical structure of the inner core in LPCs. (a, b) Low magnification and high magnification SEM images of LPCs derived nanocarbon spheres. (c) *In situ* FTIR spectra for LPCs collected at different reaction stages from 10 s to 2 h. (d) TEM image of LPCs after leached by HCl solution. (e) MALDI-TOF mass spectrum of composition released from the inner core of LPCs. (f) DSC curves of LPCs. The SEM images in (a, b) and TEM image in (d) were collected at room temperature.

As mentioned above, the nanocarbon spheres with surface folds can be either in interlinked patterns or in dispersed powder form. When we thermally treat the dispersed polymer spheres in the powder state, the resultant carbon spheres are highly uniform in size and the gyrus-like surface folds are well maintained (**Figure 2a, b**). Of notice, our method is facile and versatile. The size and surface topography of the carbon nanospheres can be precisely controlled simply by adjusting the polymerization temperature. Specifically, as the temperature increases from 25 °C to 90 °C, the diameter of obtained carbon nanospheres can be continuously tuned from 270 nm to 460 nm with high size uniformity. Concurrently, the folding depth on the carbon sphere surface could be synchronously modulated from 10 nm to 40 nm under corresponding preparation conditions (**Figure S13**). This direct temperature-mediated regulation offers a simple pathway for the multiscale morphological design of functional carbon materials. In addition, we evaluated the porous structures and surface chemistry by gas adsorption using a series of molecular probes including N_2 at 77 K, CO_2 at 273 K, and H_2O

at 298 K. (**Figure S14a, b, c**). The N_2 adsorption isotherm of DPC is typically type I, indicating its microporous feature. The specific surface area was determined to be around 529 m^2 g^{-1} according to the Brunner-Emmet-Teller theory. Furthermore, the dominated pore size of DPC is distributed at 0.48 nm, which is determined based on the non-local density functional theory (**Figure S14a**). While for H_2O adsorption, it displays a sharp water uptake from the starting point to a relative humidity of 40% RH (**Figure S14c**), indicating its relatively hydrophilic feature.

To understand the formation pathway of the LPCs, we conducted *in situ* Fourier transform infrared spectroscopy (FTIR) test (**Figure 2c**). In 10 seconds, an absorption band at 1612 cm^{-1} was observed, which can be assigned to C=N stretching vibration, evidencing the fast nucleation of Schiff-base core.[42] Moreover, the C-N stretching band at 1195 cm^{-1} became obvious as the reaction continued, confirming the formation of crosslinked polybenzoxazine networks due to the co-polymerization of TPA, HQ, and *p*-PDA.[32] The C1s and N1s X-ray photoelectron spectra of LPCs also show the coexistence of C-N bonds and C=N bonds (**Figure S15**). Considering the chemical property of the Schiff-base core, we tried to extract it by dissolving in acid or organic solvents. For instance, after soaking in 0.18 M HCl solution or 1-butanol for 24 h, the soft-core was indeed leached out (**Figure 2d, Figure S16, S17**). We found that the leached nanospheres failed to form the fold structures after the identical thermal treatment, which evidenced the crucial role of the soft-core for the formation of the surface folding (**Figure S18**). Subsequently, we analyzed the extracts by matrix-assisted laser desorption ionization time-of-flight mass spectroscopy (MALDI-TOF MS). The mass distribution of the extracts is shown in **Figure 2e**. The molecular mass of the adjacent peaks is exactly with a fixed interval of 206 Dalton, which equals the molecular mass of a repeating unit of the Schiff-base. These results nicely verified the structure and composition of the soft Schiff-base core in the LPCs.

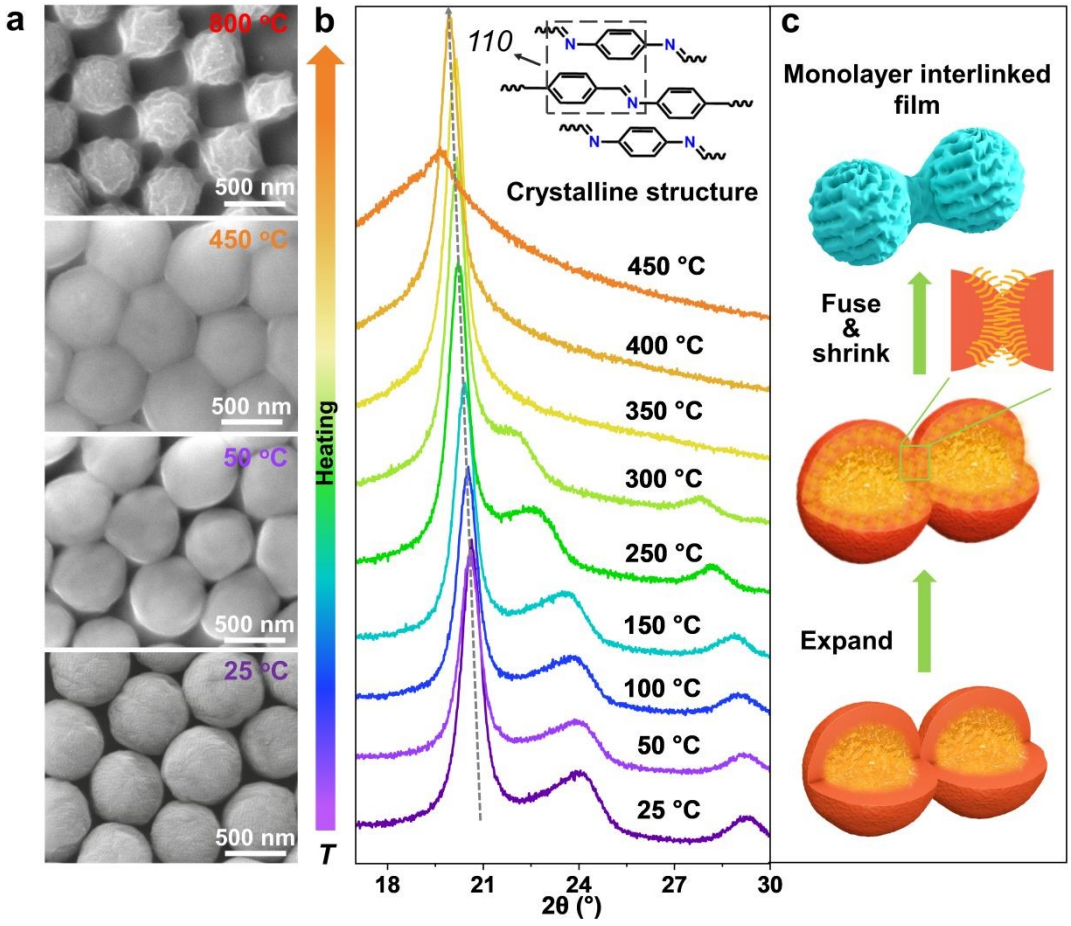

Figure 3 *In situ* visualization of the dynamic structure evolution during thermal treatment and the proposed linking mechanism. (a) *In situ* SEM images collected at 20 °C, 50 °C, 450 °C, and 800 °C during the thermal transition of monolayer LPCs. Heating rate: 10 °C min^{-1}. (b) *In situ* PXRD patterns collected during heating the LPCs from 20 to 450 °C, with pauses to take a set of XRD scans at an interval of 50 °C. The dashed line indicates the shift of the peak to lower angles. Inset: the model of the crystalline structure of LPCs inner core viewing in the direction perpendicular to the chains. (c) The proposed formation process of neck-like links in MLCF.

Next, we studied the thermotropic behavior of LPCs by thermogravimetric analysis (TGA) (**Figure S19**) together with differential scanning calorimetry (DSC) (**Figure 2f**). Based on the TG curve, we speculate the conversion of LPCs experienced two stages. The weight loss in the first stage from RT to 450 °C is within 3%, which is relevant to the adsorbed water. Meanwhile, two endothermic peaks are observed at 170 °C and 261 °C in DSC curve, which can be attributed to the glass transition of stiff-shell and crystalline melting of soft Schiff-base core. Similar observations were reported on other Schiff-base polymeric crystals.[43,44] The sample experienced a

View Article Online
DOI: 10.1039/D5SC04466A

significant weight loss about 53% during the second stage of 450-1000 °C, which was due to the decomposition of polymeric molecular chains and subsequent evolution towards carbon structures. Notably, the formation of nanofolds structure started at around 500 °C, which coincides well with the TGA-DSC results.

Followingly, we conducted a thorough investigation on the formation process of MLCF. The thermal transformation emerges as a pivotal stage in creating neck-like junctions among spheres. To directly observe this process, we employed *in situ* SEM and *in situ* XRD to provide a visual insight into the thermal transformation of LPCs as well as a comprehensive picture of the MLCF formation process (**Figure 3a, b**). As shown, the monolayer of LPCs were originally hexagonally assembled on the substrate (**Figure 3a bottom**). Due to the non-standard spheroid shape of the polymer sphere, between which there left discernible gaps. Upon heating the sample to 450 °C, each PLC exhibited volume expansion and thus squeezed each other, completely filling the interstitials (**Figure 3a middle**). Further heating induced the fusion and connection of the thermotropic liquid crystals with adjacent spheres. However, the stiff shell of the LPCs prevented them from completely merging. As heating to 800 °C, the size of the obtained nanospheres shrank to 450 nm. However, each sphere was still interlinked with its neighboring spheres by the "nano-necks"; meanwhile, each sphere shows gyrus-like surface nanofolds (**Figure 3a top**).

Figure 3b provides the results of *in situ* XRD measurements during thermal treatment process. The dashed line shows the evolution of the most obvious features of the samples during thermal transformation. In the heating process of 20-450 °C, the sharp peak at 20.4° (110) moves to lower angles, due to the expansion of the unit cell (**Figure 3b inset**). Further increasing the temperature to 450 °C and above (**Figure S20**), the XRD patterns changed obviously, and the peak of 20.4° disappeared and transformed into (002) peak of graphitic carbons, indicating the formation of nanocarbon structures. Based on these data, we summarized the formation process in **Figure 3c**. In brief, the nanolinks stem from the melting of quasi-liquid crystal core. Upon heating, the melting core partly penetrated through the softening shell and fused with the neighboring. Meanwhile, the heterogeneous polymeric spheres gradually shrunk, which pulled the neighboring spheres apart. Such tension forces induced the nanowire drawing, ending with the neck-like junction among nanocarbon spheres. In contrast, we found that the carbon nanospheres derived from pure stiff polymer failed to link with the surroundings (**Figure S21**). These results reveal that the unique combination of stiff-shell and soft-core structure is crucial for the formation of such interlinked nanocarbon arrays.

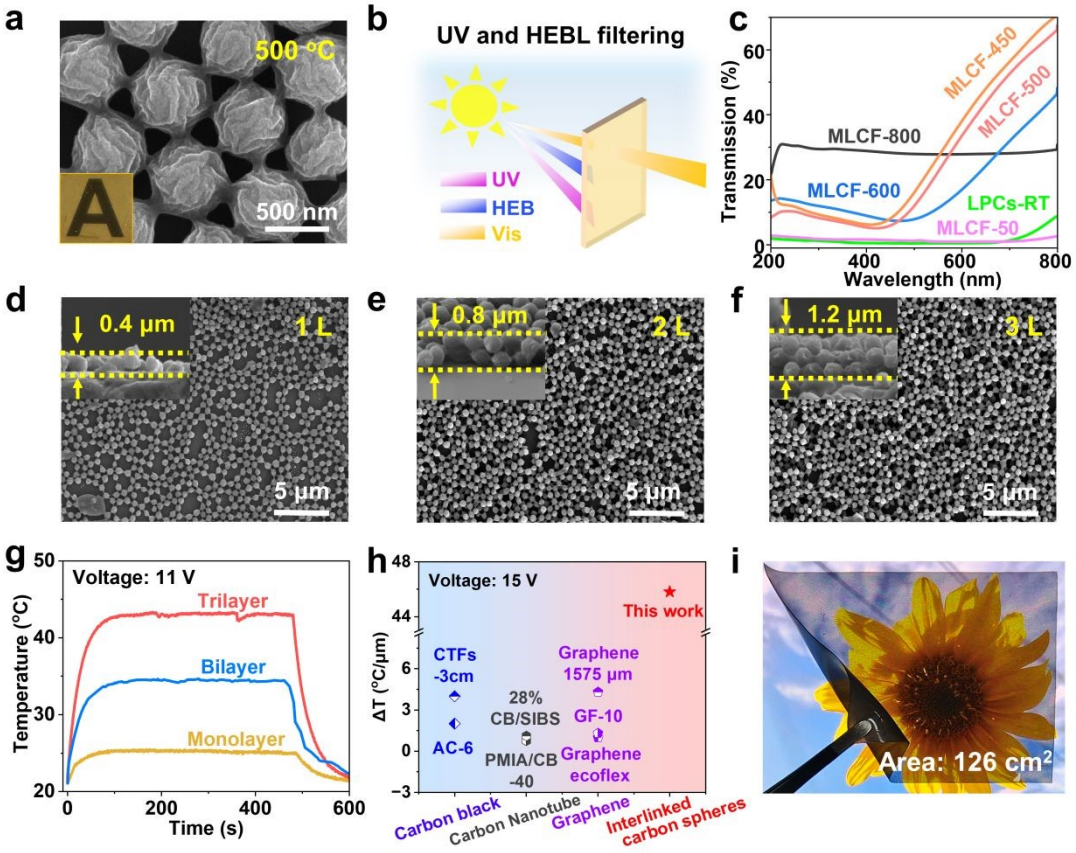

Figure 4 The UV light filtering and resistive heating properties of MLCF. (a) SEM image of MLCF prepared at 500 °C. Inset: the visible assessment of transparency of the monolayer film of MLCF-500. (b) Schematic illustration of UV light and HEBL filtering through MLCF. (c) UV–vis transmission spectra of sample LPCs-RT and thermally treated MLCF at different temperatures. SEM images of Si supported CF-1L (d), CF-2L (e), and CF-3L (f). Inset: the cross-section of the CF-1L and its 2-layer (CF-2L) and 3-layer (CF-3L) counterpart. (g) Time-dependent temperatures of MLCF with different layers with the applied potential of 11 V. (h) A performance comparison diagram of ΔT with thickness normalization for different film materials with the applied potential of 15 V.[10,46-51] (i) Optical image of flexible monolayer film of interlinked nanocarbon spheres on PDMS substrate with area of 126 cm^2. The SEM images in (a, d, e, f) and optical image in (i) were collected at room temperature.

The monolayer assembly of LPCs can easily proceed on flexible substrates such as PDMS. The evident folding surface increases the adhesion to the substrate surface, thereby warranting a high successful rate for device fabrication (**Figure S22**). The monolayer film of interlinked nanocarbon spheres in such large area motivated us to explore its application as light filters. The monolayer of LPCs underwent thermal treatment at 500 °C, yielding MLCF-500 (**Figure 4a, Figure S23**). Compared with the monolayer of LPCs without thermal treatment (**Figure S24**), the formed voids in MLCF-500 due to the volume shrinkage of LPCs during thermal treatment allow light transmitting freely (**Figure 4a inset**).

We then optimized the thermal treatment conditions (**Figure S25**), and the typical films demonstrate a high transmittance for visible light while effectively filtering most harmful UV light and high energy blue light (HEBL) (**Figure 4b**). Among the tested samples, MLCF-450 and MLCF-500 demonstrated favorable filtration capabilities toward both UV and HEBL. In contrast, MLCF-50 was largely impermeable to these wavelengths, and MLCF-800 failed to selectively shield UV light and HEBL. The excellent performance of MLCF-500 is ascribed to its appropriate preparation temperature, which preserves the aromatic ring in the polymer as well as the C–N/C=O bonds. These functionalities enable efficient absorption of UV light radiation and subsequent conversion of its energy into heat and fluorescence via π→π* transitions in the conjugated aromatic system and n→π* transitions related to carbon–heteroatom bonds (**Figure S26**).[45] As a result, MLCF-500 achieved a high transmittance for visible light while blocking 90% and above UV light and HEBL (**Figure 4c**), making it promising for optical applications.

In addition, the large area monolayer film exhibited consistent optical performance after exposure to high-power UV light irradiation for 72 h (**Figure S27**). Even after immersing in water at different temperatures, the UV light transmittance of MLCF-500 only increased slightly by 1.2% (**Figure S28**). The outstanding durability is ascribed to the inherent stability of carbon materials. Furthermore, we investigated the effect of the incident angle of light. As the light incident varied from 6 to 76 degrees, the transmission of light in both UV light and visible spectra decreased to some extent. However, it maintains over 90% absorption of UV light as well as considerable transparency in all the conditions (**Figure S29**). To our knowledge, this is the first demonstration that large-area transparent monolayer film of interlinked nanocarbon spheres can be used for UV light protection. This might be useful for biological protection from UV light damage.

Due to the excellent conductivity and ultrathin properties of MLCF, we further investigated its potential application as resistive heating materials. By repeating the single-layer assembly process of LPCs, carbon film resistance heaters with an area of 24 cm^2 and different layers (**Figure 4d-f, S30, S31**) were successfully fabricated and named CF-1L, CF-2L, and CF-3L in turn. The electrothermal performance tests demonstrated that when a voltage of 11 V was applied across a 3.0 cm × 3.0 cm sample, the surface temperature of only 1.2 μm thick CF-3L rapidly reached 43 °C (**Figure 4g**). Furthermore, we observed that as the number of MLCF layers increased, the electrical heating performance of the resistance heater increased regularly. Specifically, for every 0.4 μm increase in thickness, the surface temperature increased by about 9 °C (**Figure S32**).

The repeatability over successive heating-cooling cycles is critical for the practical application of wearable heaters. The CF-3L heater consistently reached a maximum temperature of approximately 70 °C over 12 cycles under alternately switching on/off 18 V, with no significant performance degradation **(Figure 33a)**. The corresponding SEM image confirmed the structural integrity after heating-cooling cycles **(Figure S33b)**. This demonstrates electrothermal stability and mechanical robustness of the device.

Figure S34 further showed that the surface temperature of CF-3L was proportional to the square of the applied voltage, following Joule's law ($Q=U^2R^{-1}t$), providing a theoretical basis for accurate temperature control of resistance heaters. It is important to note that CF-3L exhibited both efficient heat generation under low-voltage conditions (< 36 V) and guaranteed operational safety (**Figure S35**). Compared with the previously reported non-metallic ultrathin Joule heating materials, MLCF demonstrated significant advantages in terms of thickness control and thermal conductivity (**Figure 4h, Table S1**). In addition, the material preparation process exhibited good scalability, and its dimension was primarily constrained by the substrate area and heat treatment furnace capacity. For example, we have successfully prepared large area MLCF samples with dimension up to 21.0 cm × 6.0 cm (**Figure 4i**).

Conclusions

We demonstrated a facile fabrication of large-area conductive porous film of interlinked nanocarbon spheres derived from quasi-liquid polymeric crystals with hybrid core-shell structure. Such core-shell structure was prepared via cascading polymerization strategy that allows the surface evolution toward nanofolds morphology. The conductive and flexible films based on interlinked monolayer nanocarbons can serve as ideal candidates for optical materials such as UV light filtering glasses and electrically heated materials such as wearable heating devices. This scalable solution synthesis and the facile transformation represent a smart engineering platform at nanoscale for the design of electronic skin and intelligent wearable devices.

Author contributions

A.-H. L. and G.-P. H. conceived presented idea and directed the project. M.-Q. Z., T.-Y. L. and C.-B. L. carried out the experiments with support from H.-Q. H., Y.-S. W., L.-Y. D., X.-D. S. and Y.-T. W., who helped preparing and characterizing samples with SEM, TEM and *in situ* XRD and analysed the data. All authors discussed the results and contributed to the final manuscript.

Conflicts of interest

The authors declare no conflict of interest.

Data availability

All the data can be found within the manuscript and ESI files.‡

View Article Online
DOI: 10.1039/D5SC04784A

Acknowledgements

This work was supported by National Natural Science Funds of China (No. 22275027), and the Fundamental Research Funds for the Central Universities (No. DUT22LAB607).

Notes and references

1 T. Cui, D. Li, T. Hirtz, J. Xu, Y. Qiao, H. Xu, H. Tian, H. Liu, Y. Yang and T. Ren, *Carbon Future*, 2024, **1**, 9200005.
2 Y. Meng, J. Feng, S. Han, Z. Xu, W. Mao, T. Zhang, J. S. Kim, I. Roh, Y. Zhao, D. Kim, Y. Yang, J. Lee, L. Yang, C. Qiu and S. Bae, *Nat. Rev. Mater.*, 2023, **8**, 498-517.
3 A. T. Hoang, L. Hu, B. J. Kim, T. T. N. Van, K. D. Park, Y. Jeong, K. Lee, S. Ji, J. Hong, A. K. Katiyar, B. Shong, K. Kim, S. Im, W. J. Chung and J. Ahn, *Nat. Nanotechnol.*, 2023, **18**, 1439-1447.
4 D. Ren, C. Zhao, S. Zhang, K. Zhang and F. Huang, *Adv. Funct. Mater.*, 2023, **33**, 2300517.
5 X. Wang, T. Liu, F. Sun, J. Zhang, B. Yao, J. Xu and J. Fu, *Smart Molecules*, 2024, **2**, e20240008.
6 C. Toh, H. Zhang, J. Lin, A. S. Mayorov, Y. Wang, C. M. Orofeo, D. B. Ferry, H. Andersen, N. Kakenov, Z. Guo, I. H. Abidi, H. Sims, K. Suenaga, S. T. Pantelides and B. Özyilmaz, *Nature*, 2020, **577**, 199-203.
7 L. Hou, X. Cui, B. Guan, S. Wang, R. Li, Y. Liu, D. Zhu and J. Zheng, *Nature*, 2022, **606**, 507-510.
8 M. Ramezani, J. Kim, X. Liu, C. Ren, A. Alothman, C. De-Eknamkul, M. N. Wilson, E. Cubukcu, V. Gilja, T. Komiyama and D. Kuzum, *Nat. Nanotechnol.*, 2024, **19**, 504-513.
9 J. Liu, N. P. Wickramaratne, S. Z. Qiao and M. Jaroniec, *Nat. Mater.*, 2015, **14**, 763-774.
10 D. Zhang, S. Xu, X. Zhao, W. Qian, C. R. Bowen and Y. Yang, *Adv. Funct. Mater.*, 2020, **30**, 1910809.
11 Y. Chu, L. Sun, J. Wang, Z. Han, C. Wei, C. Han and H. Yan, *Nanomaterials*, 2024, **14**, 911.
12 M. Ghasemlou, N. PN, K. Alexander, A. Zavabeti, P. C. Sherrell, E. P. Ivanova, B. Adhikari, M. Naebe and S. K. Bhargava, *Adv. Mater.*, 2024, **36**, 2312474.
13 X. Ma, Q. Liu, N. Yu, D. Xu, S. Kim, Z. Liu, K. Jiang, B. M. Wong, R. Yan and M. Liu, *Nat. Commun.*, 2021, **12**, 6868.
14 Z. Wang, X. Kong, Y. Huang, J. Li, L. Bao, K. Cao, Y. Hu, J. Cai, L. Wang, H. Chen, Y. Wu, Y. Zhang, F. Pang, Z. Cheng, P. Babor, M. Kolibal, Z. Liu, Y. Chen, Q. Zhang, Y. Cui, K. Liu, H. Yang, X. Bao, H. Gao, Z. Liu, W. Ji, F. Ding and M. Willinger, *Nat. Mater.*, 2024, **23**, 331-338.
15 Y. Zhao, X. Yang, Z. Cheng, C. H. Lau, J. Ma and L. Shao, *Nat. Commun.*, 2023, **14**, 2679.
16 S. Rahman, T. Yildirim, M. Tebyetekerwa, A. R. Khan and Y. Lu, *ACS Nano*, 2022, **16**, 13959-13968.
17 S. Lim, E. Jang, D. Yu, J. Koo, D. Kang, K. M. Lee, N. P. Godman, M. E. McConney, D. Kim and K. Jeong, *Adv. Mater.*, 2023, **35**, 2206764.
18 Y. Liu, Z. Feng, C. Xu, A. Chatterjee and A. A. Gorodetsky, *ACS Nano*, 2021, **15**, 17299-17309.
19 T. Ma, T. Li, L. Zhou, X. Ma, J. Yin and X. Jiang, *Nat. Commun.*, 2020, **11**, 1811.
20 L. Peng, C. Hung, S. Wang, X. Zhang, X. Zhu, Z. Zhao, C. Wang, Y. Tang, W. Li and D. Zhao, *J. Am. Chem. Soc.*, 2019, **141**, 7073-7080.
21 L. Liu, S. Xu, Q. Yu, F. Wang, H. Zhu, R. Zhang and X. Liu, *Chem. Commun.*, 2016, **52**, 11693-11696.
22 Z. Zhao, Y. Huang, J. Du and A. Chen, *Chem. Asian J.*, 2023, **18**, e202300486.
23 Y. Sun, C. Li, D. Liu, F. Zhang, J. Xue and Q. Zheng, *ACS Nano*, 2025, **19**, 1944-1980.
24 J. Jang, H. Choo, S. Lee, J. Song, K. Park, J. Yoon, D. Seong, S. An, H. Jung, J. Ju, J. Kang, J. Kang, I. S. Kim, M. Shin, J. Park and D. Son, *Nat. Electron.,* 2025, https://doi.org/10.1038/s41928-025-01389-z.
25 Y. Yue, D. Zhang, P. Wang, X. Xia, X. Wu, Y. Zhang, J. Mei, S. Li, M. Li, Y. Wang, X. Zhang, X. Wei, H. Liu and W. Zhou, *Adv. Mater.,* 2024, **36**, 2313971.
26 S. Arimura, I. Matsumoto, R. Sekiya and T. Haino, *Angew. Chem. Int. Ed.,* 2024, **63**, e202315508.
27 L. Yu, L. Liang, I. Bajaj, K. Seabright, D. J. Keffer, I. N. Ivanov, H. Chen, S. Dai, A. J. Ragauskas, C. T. Maravelias and D. P. Harper, *Carbon*, 2023, **213**, 118285.
28 M. Kim, R. Xin, J. Earnshaw, J. Tang, J. P. Hill, A. Ashok, A. K. Nanjundan, J. Kim, C. Young, Y. Sugahara, J. Na and Y. Yamauchi, *Nat. Protoc.*, 2022, **17**, 2990-3027.
29 R. Li, B. Ma, M. Li, D. Wang, P. Liu and P. An, *Chem. Sci.*, 2024, **15**, 11408-11417.
30 J. Uchida, B. Soberats, M. Gupta and T. Kato, *Adv. Mater.*, 2022, **34**, 2109063.
31 H. K. Bisoyi and Q. Li, *Chem. Rev.*, 2022, **122**, 4887-4926.
32 S. Wang, W. Li, G. Hao, Y. Hao, Q. Sun, X. Zhang and A. Lu, *J. Am. Chem. Soc.*, 2011, **133**, 15304-15307.
33 Z. Zheng, M. Wu, X. Zeng, X. Zhu, D. Luo, X. Chen, Y. Chen, G. Yang, D. Bin, X. Zhou and D. Li, *Angew. Chem. Int. Ed.*, 2024, **63**, e202400012.
34 Y. Pi, L. Cui, W. Luo, H. Li, Y. Ma, N. Ta, X. Wang, R. Gao, D. Wang, Q. Yang and J. Liu, *Angew. Chem. Int. Ed.*, 2023, **62**, e202307096.
35 J. L. Segura, M. J. Mancheño and F. Zamora, *Chem. Soc. Rev.*, 2016, **45**, 5635-5671.
36 T. J. White and D. J. Broer, *Nat. Mater.*, 2015, **14**, 1087-1098.
37 B. Crist and J. M. Schultz, *Prog. Polym. Sci.*, 2016, **56**, 1-63.
38 W. Łużny, E. Stochmal-Pomarzańska and A. Proń, *Polymer*, 1999, **40**, 6611-6614.
39 T. Tallinen, J. Y. Chung, J. S. Biggins and L. Mahadevan, *Proc. Natl. Acad. Sci. U.S.A.*, 2014, **111**, 12667-12672.
40 I. Tobasco, Y. Timounay, D. Todorova, G. C. Leggat, J. D. Paulsen and E. Katifori, *Nat. Phys.*, 2022, **18**, 1099-1104.
41 F. Xu, Y. Huang, S. Zhao and X. Feng, *Nat. Comput. Sci.*, 2022, **2**, 632-640.
42 F. Jin, T. Wang, H. Zheng, E. Lin, Y. Zheng, L. Hao, T. Wang, Y. Chen, P. Cheng, K. Yu and Z. Zhang, *J. Am. Chem. Soc.*, 2023, **145**, 6507-6515.
43 G. Chen, B. Jin, Y. Shi, Q. Zhao, Y. Shen and T. Xie, *Adv. Mater.*, 2022, **34**, 2201679.
44 S. T. Ha, L. K. Ong, S. T. Ong, G. Y. Yeap, J. P. W. Wong, T. M. Koh and H. C. Lin, *Chin. Chem. Lett.*, 2009, **20**, 767-770.

45 B. K. Barman, Ø. Sele Handegård, A. Hashimoto and T. Nagao, *ACS Sustain. Chem. Eng*., 2021, **9**, 9879-9890.
46 Y. Wang, X. Ding, H. Wang, Q. Wang, M. Zhang and B. Yang, *ACS Appl. Polym. Mater*., 2024, **6**, 7612-7620.
47 J. Luo, H. Lu, Q. Zhang, Y. Yao, M. Chen and Q. Li, *Carbon*, 2016, **110**, 343-349.
48 H. Song, B. Nie, Y. Zhu, G. Qi, Y. Zhang, W. Peng, X. Li, J. Shao and R. Wei, *Langmuir*, 2024, **40**, 6940-6948.
49 Z. Shao, Y. Liu, P. Cai, Q. Wang, Z. Xiao, L. Zhang, B. Tong, B. Wang, Y. Zhao, W. Zhang and Y. Xia, *J. Electron. Mater.*, 2024, **53**, 4601-4612.
50 H. Weerathunga, T. T. Do, H. D. Pham, R. Jones, J. MacLeod, T. Kim and D. Dubal, *Adv. Mater. Technol*., 2023, **8**, 2201538.
51 Y. Liu, Z. Xiao, W. Zhang, H. Huang, J. Zhang, Y. Gan, X. He, B. Wang, Y. Han and Y. Xia, *J. Ind. Eng. Chem*., 2022, **107**, 401-409.

View Article Online DOI: 10.1039/D5SC04466A

Journal Name ARTICLE

View Article Online
DOI: 10.1039/D5SC04466A

Data availability

All the data can be found within the manuscript and ESI files.‡